



Correlation between the shear-speed structure and thickness of the mantle transition zone

Sergei Lebedev^{a,*}, Sébastien Chevrot^b, R.D. van der Hilst^c

^a MIT, EAPS, Room 54-512, Cambridge, MA 02139, USA

^b Observatoire Midi Pyrénées, 14 Avenue Edouard Belin, 31400 Toulouse, France

^c MIT, EAPS, Room 54-514, Cambridge, MA 02139, USA

Received 28 October 2001; received in revised form 27 June 2002; accepted 23 July 2002

Abstract

The 410 and 660 km seismic discontinuities that bound the mantle transition zone (TZ) are attributed to phase transformations in olivine structure. This implies that variations in TZ thickness (H_{TZ}) should correlate with those in TZ temperature. Pertinent seismic evidence has so far been ambiguous, however. We measure converted-wave (Pds) differential times $t_{diff} = t_{P660s} - t_{P410s}$ in SE Asia and Australia and compare them with S -velocity (β_{TZ}) estimates from regional tomographic models. Both t_{diff} and β_{TZ} vary on a scale of a few hundred kilometers. Inferred variations in H_{TZ} are up to ± 30 km over length scales larger than 500 km, implying ± 200 K thermal heterogeneity if the effect of composition can be neglected. t_{diff} and β_{TZ} correlate strongly; the linear dependence of H_{TZ} on the average temperature within the TZ is consistent with olivine Clapeyron slopes. We also show that this relationship holds on a global-scale as well, provided that the scalelengths and uncertainties of the variations in t_{diff} and β_{TZ} are taken into account. These results confirm that the transformations in olivine structure give rise to the 410 and 660 km discontinuities globally.

© 2003 Elsevier Science B.V. All rights reserved.

Keywords: Discontinuities; Converted waves; Receiver functions; Tomography; Clapeyron slopes; Olivine

1. Introduction

Accurate constraints on the properties of the transition zone discontinuities are necessary for the understanding of the patterns of the mantle flow as well as the very composition of the mantle. Owing to observational difficulties, current models are characterized by large uncertainties, and even their basic features are debated (e.g. [Irfune et al., 1998](#); [Shim et al., 2001](#)).

The mantle transition zone (TZ) is bounded by two sharp seismic discontinuities at approximately 410 and 660 km depth. According to the most commonly accepted view ([Fig. 1](#)) the discontinuities (410 and 660) are due to phase transformations in olivine, in an olivine-dominated mantle. For a typical mantle adiabat, the olivine-wadsleyite transition ($\alpha \rightarrow \beta$) occurs at pressures corresponding to 410 km depth and it is thought to be the cause of the jump in the elastic properties of the mantle rock observed at the depth. The break-down of the spinel phase (ringwoodite) into perovskite and magnesiowüstite ($sp \rightarrow pv + mw$, also referred to as the post-spinel transformation) has been observed at conditions that occur near 660 km depth in the mantle and is thought to be the cause of

* Corresponding author. Fax: +1-617-258-9697.

E-mail addresses: sergei@quake.mit.edu (S. Lebedev), Sebastien.Chevrot@cnes.fr (S. Chevrot), hilst@mit.edu (R.D. van der Hilst).

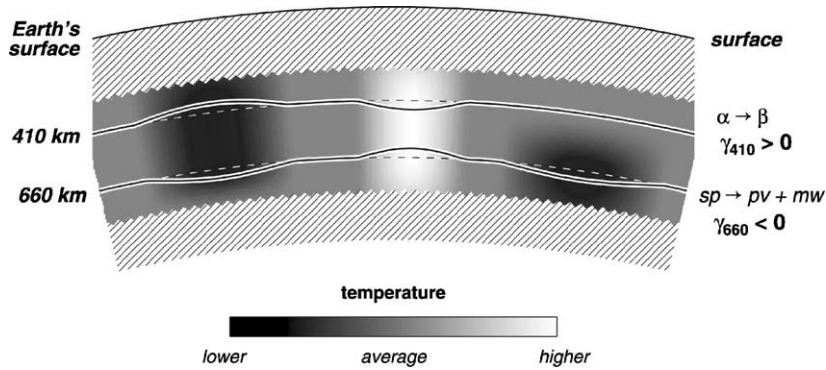


Fig. 1. Schematic depiction of the transition zone in an olivine-dominant mantle. Low temperatures cause a thickening of the transition zone; high temperatures—a thinning.

the 660 (Bernal, 1936; Anderson, 1967; Ringwood, 1969).

An important characteristic of a phase transformation is its Clapeyron slope γ , which is the temperature derivative of the pressure at which the transformation occurs ($\gamma = dP/dT$). In the Earth, changes of the pressure of the transition will translate into changes of its depth, so that lateral variations in temperature can create topography on the seismic discontinuity. The Clapeyron slope of the $\alpha \rightarrow \beta$ transformation is positive (Suito, 1977; Katsura and Ito, 1989), so that a low-temperature anomaly will cause a local uplift of the 410 km discontinuity, whereas a high-temperature anomaly will cause a depression. The slope of the $sp \rightarrow pv + mw$ transformation is probably negative (Navrotsky, 1980; Ito and Takahashi, 1989), implying a depression of the 660 km discontinuity in a low-temperature environment and an uplift at high temperatures.

This view is supported by mineralogical and seismological observations (e.g. Ito and Takahashi, 1989; Katsura and Ito, 1989; Bina and Helffrich, 1994; Weidner and Wang, 2000; Helffrich, 2000; Shearer, 2000), which, despite their rather large uncertainties are often taken for granted. The origin and properties of the discontinuities, however, are still enigmatic, owing to the difficulty in making the pertinent seismic and mineralogical measurements.

Phase transformations in the Earth occur over finite depth intervals in which multiple phases co-exist, so that Clapeyron slopes at 410 or 660 cannot be defined thermodynamically (Bina and Helffrich,

1994). Finite-frequency seismic waves, however, see the discontinuities as sharp interfaces. By using seismic measurements of the depths to these apparent interfaces, one could constrain “effective” Clapeyron slopes at the discontinuities. Bina and Helffrich (1994) refer to them as “seismic” Clapeyron slopes and note that, except for a slight dependence on the seismic-wave frequency, they otherwise depend only on thermodynamic properties. By using seismic observables sensitive to pressure and temperature at the discontinuities and neglecting, as an initial assumption, possible effects of compositional heterogeneity on these observables, one could constrain the effective Clapeyron slopes.

Arrival times of seismic waves converted or reflected at 410 or 660 depend on (and can be used to constrain) lateral variations in the depth to the discontinuities (or the pressure of the corresponding phase transformation). The values of seismic velocities in the TZ can be used to infer temperature variations, with conversion factors from experimental and theoretical mineral physics. The effective Clapeyron slopes can thus be constrained with these two types of data.

Unfortunately, both types of seismic measurement are difficult to make in practice and, moreover, are not independent. Although many tomographic models map seismic heterogeneity in the TZ, the wavespeed values are uncertain (e.g. Becker and Boschi, 2002). Topography on the discontinuities have been measured using different approaches, often with conflicting results (see Shearer, 2000 and Helffrich, 2000 for

reviews). Most previous studies have relied on crude estimates of the upper-mantle seismic-velocity structure in order to convert the arrival time of a pertinent seismic phase into the depth to a discontinuity. In addition, the topography and seismic heterogeneity are often measured with different lateral resolution which can distort or conceal existing correlation patterns.

In this study, we use the results of recent high-resolution tomographic studies of SE Asia and Australia and combine them with measurements of the converted-wave (Pds) delay times. The tomographic models were computed using large waveform data sets with substantial resolving power in the transition zone. We do not, however, take the tomographically derived S -velocities at face value, but instead perform extensive testing and derive robust estimates of the S -velocity values and their uncertainties in the TZ beneath the stations of the Pds dataset. The tomography and Pds analysis both achieve a lateral resolution in the TZ of about 500–600 km. Subsequently, we attempt to extend our analysis to global-scale using published global tomographic models.

2. Previous studies: approaches and results

2.1. Short-period, near-source phases

The analysis of short-period waves generated from deep subduction-zone earthquakes and reflected or converted from discontinuities near the source (e.g. Vidale and Benz, 1992; Wicks and Richards, 1993; Collier and Helffrich, 1997; Castle and Creager, 1998) has a number of advantages. First, it offers a high lateral resolution (resolution length of 100 km or less). Second, the temperature in subducting slabs can be estimated roughly from the age and descent rate of the cold oceanic lithosphere. Both local uplift of 410 and depression of 660 have been observed, with their magnitude generally consistent with the olivine-transformation origin of the discontinuities. Subduction zones, however, represent a small fraction of the upper-mantle, characterized by extremely large temperature anomalies, and it is not certain to what extent the properties of the discontinuities in these regions are representative of those elsewhere in the Earth.

2.2. Long-period reflections

The best global coverage has been achieved in the studies using underside reflections of long-period shear waves (e.g. Gössler and Kind, 1996; Flanagan and Shearer, 1998; Gu et al., 1998). However, the data sampling is achieved at the expense of lateral resolution, which is often difficult to quantify. ScS reverberations (e.g. Revenaugh and Jordan, 1991) have been used in regional-scale studies. Absolute discontinuity depths are determined from differential travel times between reflected phases and a reference phase (e.g. SS) using rays traced in seismic models of the crust and upper-mantle in the region of the reflection points. Because uncertainties in the models of the highly heterogeneous upper-mantle can translate into substantial errors of the inferred discontinuity topography, the thickness of the TZ (H_{TZ}) can be measured more accurately (using underside-reflection differential times) than the topography on either 410 or 660. Finally, long-period seismic phases used in the studies have broad and complex sensitivity volumes (e.g. Hung et al., 2000; Zhao et al., 2000). Ray-theoretical interpretation of the differential travel times can be significantly in error (Neele et al., 1997) for discontinuity topography on a scale of a few hundred kilometers (such as in subduction zones). Chaljub and Tarantola (1997) suggested that uplifts and depressions of the 660 can be retrieved correctly from t_{SS} to t_{S660S} delays only at length scales larger than 1500 and 3000 km, respectively. Shearer et al. (1999) argued that if the data coverage is dense and sufficient lateral averaging is applied, the presence of small-scale topography does not cause a significant bias in the maps of large-scale discontinuity topography and TZ thickness variations.

The correlation of global maps of H_{TZ} obtained using SS precursors with tomographic TZ wavespeeds is roughly consistent with the olivine Clapeyron slopes (Flanagan and Shearer, 1998) but is unexpectedly low.

2.3. Short-period near-receiver conversions

In contrast to the long-period underside reflections, short-period P -to- S conversions on the receiver side offer lateral resolution of a few hundred kilometers. With this technique, data coverage directly reflects the distribution of broad band stations (e.g. Bostock,

1996; Dueker and Sheehan, 1997; Gurrola and Minster, 1998; Li et al., 2000) and is best in continental regions, in particular, Eurasia and North America. Sampling of oceanic mantle has been poor, but this should be improved with ocean-bottom seismometer deployments.

Chevrot et al. (1999) performed a global-scale study of Pd s travel times, supplementing new measurements with those from earlier studies. Their analysis showed that variations in the absolute $P410s$ and $P660s$ arrival times are dominated by the impact of seismic heterogeneity above 410 and that the discontinuity topography has only a second-order effect. To determine the absolute depth to a discontinuity from the converted-phase arrival times it is necessary to have a very accurate tomographic model of the upper-mantle for both P and S velocities. The differential travel times $t_{diff} = t_{P660s} - t_{P410s}$, however, are not sensitive to the structure above 410 and can be used to constrain the TZ thickness.

The comparison of t_{diff} with the seismic velocities in the TZ taken from global tomographic models (Su et al., 1994; Grand et al., 1997; Van der Hilst et al., 1997) showed poor correlation (Chevrot et al., 1999), a surprising result because the olivine-transformation model predicts strong effects of temperature on both the velocities and discontinuity topography (Fig. 1). Here we suggest that the discrepancy is mostly due to differences in spatial resolution as well as uncertainties of the data compared.

3. Converted-wave analysis

Pd s phases are the arrivals of the waves converted from P to S at a discontinuity at depth d , in this study either 410 or 660 km (Fig. 2). Our analysis is based on the approach first introduced by Vinnik (1977). For the data processing we follow Chevrot et al. (1999).

3.1. t_{P410s} and t_{P660s} measurements

For each station, we collect all available traces and—in an initial visual selection—reject those with strong background noise before the P onset. Each three-component seismogram is then transformed into a series of “bumps” by means of rotation and deconvolution by the principal component of the recorded

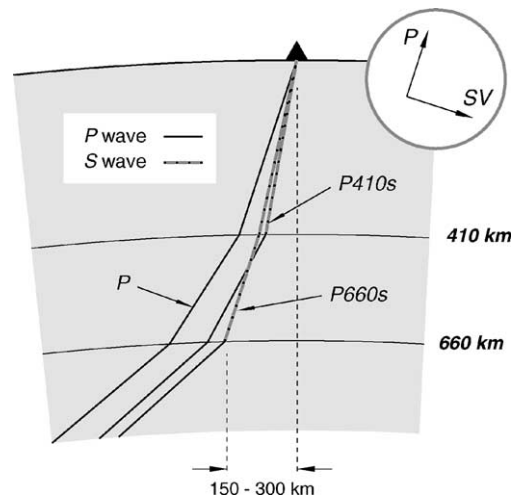


Fig. 2. Schematic ray diagram of the P , $P410s$, and $P660s$ phases. The triangle denotes a seismic station on the Earth's surface. The axes P and SV (top right) are in the direction of the P and SV waves particle motion.

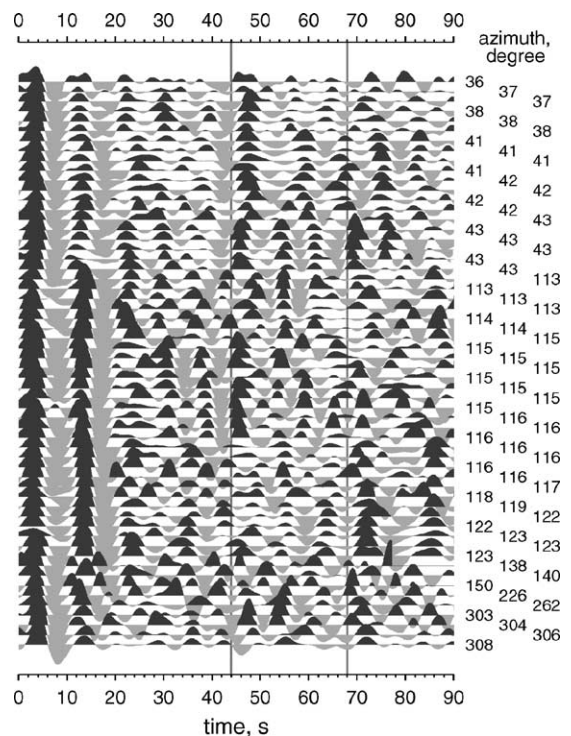


Fig. 3. Fifty-eight processed traces at the station QIZ, low-pass filtered at 8 s and ordered by azimuth. The global-average arrival times of $P410s$ and $P660s$ are shown with vertical lines, at 44 and 68 s, respectively.

P-wave train, with a move-out correction depending on the slowness of the *P*-wave. Traces with a prominent phase (e.g. *PcP* or *PP*) in the coda of the *P*-wave and those with the *SV*-component amplitude exceeding an empirical threshold of 15% of the *P*-wave amplitude are discarded. Usually, the *P*_{*d*} phases are not clearly visible on all individual traces (Fig. 3). The arrival times t_{P410s} and t_{P660s} are measured on the stacks of all traces (Fig. 4), relative to the arrival of the *P*-wave, with measurement errors determined using bootstrap analysis (Efron and Tibshirani, 1991).

In addition to low signal-to-noise ratios (typically, at ocean-island and portable stations), reasons for data rejection include complexity of the traces due to strong upper-mantle heterogeneity or small-scale topography on the discontinuities (e.g. in active subduction zones), and insufficient numbers of available records for a meaningful error analysis (temporary or recently installed stations).

Since we stack the records produced by events at different azimuths and distances, the piercing points of the waves at the discontinuities are distributed over an

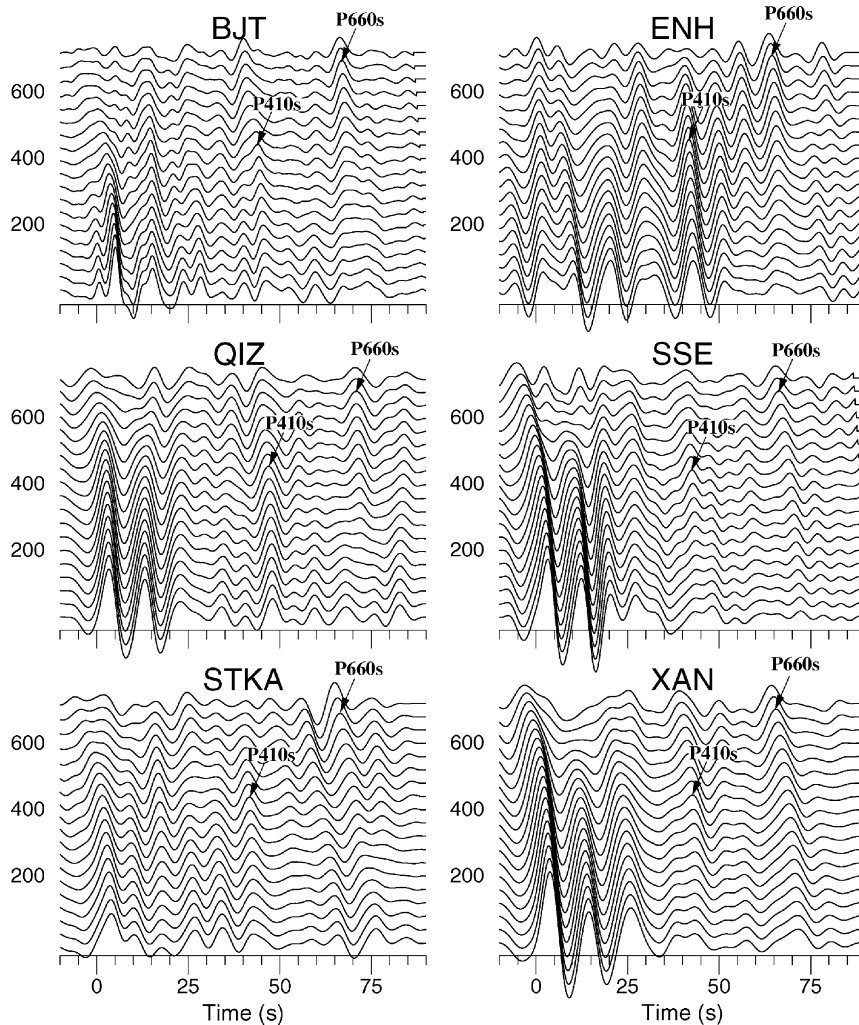


Fig. 4. Depth stacks at six stations. The vertical-scale is depth (km). The time of the converted-phase arrival corresponds to the top of its bump and is measured relative to *P* (0s). All traces in our dataset are low-passed at 6 s, except for those from the stations QIZ and STKA (8 s).

area of finite width beneath the station (Fig. 2). Taking into account the 100–300 km width of the Fresnel zone of the waves at the the discontinuities (see Chevrot et al., 1999 for discussion), we estimate the lateral resolution of the measurements at around 500–600 km.

3.2. Differential times t_{diff}

Below the discontinuity d (Fig. 2), the paths of the P and P_d s waves are virtually identical to one another, and to first-order the relative arrival time t_{P_d} s depends only on the depth to the discontinuity d and the P - and S -velocity structure above it.

Our tomographic models represent S but not P velocities. In the absence of reliable constraints on P -wave speed we do not attempt to estimate the absolute values of the depths to the discontinuities (d_{410} and d_{660}). In principle, P -velocity anomalies ($\delta\alpha$) can be estimated from S -velocity anomalies ($\delta\beta$) if the ratio $R = \delta \ln \beta / \delta \ln \alpha = (\delta\beta/\beta)/(\delta\alpha/\alpha)$ is known. Unfortunately, applicability of this estimate is questionable in the upper 200–300 km of the mantle, where lateral variations in R are expected to be strong (e.g. Goes et al., 2000). Since the shallow seismic structure has the largest contribution to the $t_{P_{410s}}$ and $t_{P_{660s}}$ variations, errors due to the assumption of constant R could be comparable in magnitude to or exceed the actual lateral variations of d_{410} and d_{660} .

Without measuring the absolute depths to 410 and 660 we can still obtain constraints on transition zone structure in the form of the differential times $t_{\text{diff}} = t_{P_{660s}} - t_{P_{410s}}$. As evident from Fig. 2, the paths of P_{660s} and P_{410s} are essentially the same below 660 km and above 410 km so that t_{diff} depends only on the thickness of the transition zone and seismic velocities in it. With this approach we have one constraint per station (t_{diff}), but we can use only the stations with robust measurements of both $t_{P_{410s}}$ and $t_{P_{660s}}$.

Fig. 5 shows the stations in the region covered by the tomographic models at which both $t_{P_{410s}}$ and $t_{P_{660s}}$ were measured successfully, along with the rest of the stations in the area. The set of measurements (Table 1) contains no values from island-arc stations on the top of subduction zones, a result of strong upper-mantle heterogeneity and small-scale discontinuity topography (e.g. Castle and Creager, 1998). There are only a few data points from the numerous stations of the portable SKIPPY array (Van der Hilst

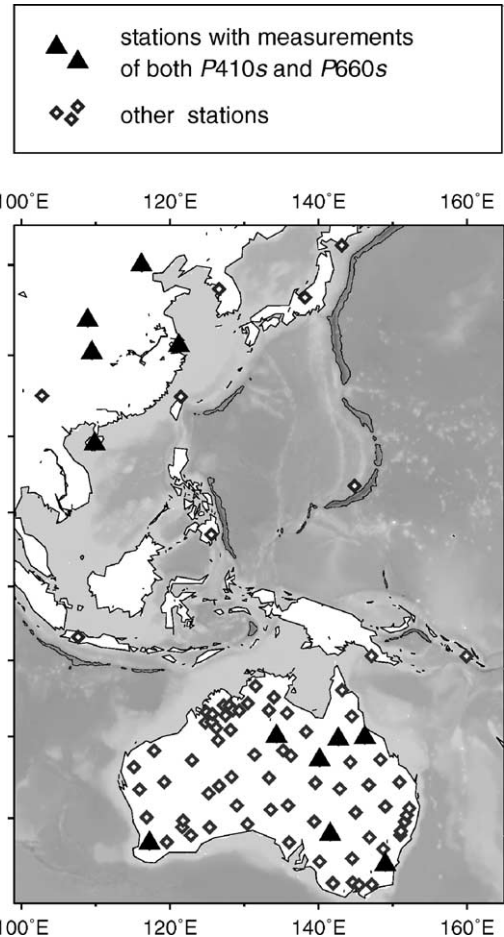


Fig. 5. Broadband stations in SE Asia and Australia.

et al., 1994) owing to the short time of instrument deployment at each location (~ 5 months) and relatively low signal-to-noise ratios at the periods considered here.

Important characteristics of the final set of measurements are that the values average laterally over 500–600 km and that the depths to the discontinuities do not change strongly within this range beneath the stations.

4. Tomographic constraints

Our upper-mantle, S -velocity models for SE Asia (Lebedev and Nolet, 2000) and Australia (Zielhuis and van der Hilst, 1996; Simons et al., 1999; Van

Table 1
Travel times of the converted phases (seconds)

No.	Station	Latitude	Longitude	t_{P410s}	t_{P660s}	t_{diff}	N_{traces}	Reference
1	BJT	40.02	116.17	45.6 ± 0.2	69.7 ± 0.3	24.1	82	This study
2	CAN	-35.32	149.00	45.0 ± 0.4	68.6 ± 0.1	23.6	135	Chevrot et al. (1999)
3	CTAO	-20.09	146.25	44.4 ± 0.3	69.2 ± 0.2	24.8	56	Chevrot et al. (1999)
4	ENH	30.27	109.49	42.8 ± 0.4	67.2 ± 0.6	24.4	35	This study
5	NWAO	-32.93	117.23	44.0 ± 0.5	66.8 ± 0.8	22.8	55	Chevrot et al. (1999)
6	QIZ	19.03	109.84	47.2 ± 0.6	70.4 ± 0.5	23.2	31	This study
7	SA03	-20.34	142.67	44.4 ± 0.5	68.6 ± 0.1	24.2	13	This study
8	SA04	-22.94	140.14	43.0 ± 0.2	66.5 ± 0.5	23.5	15	This study
9	SSE	31.10	121.19	44.2 ± 0.1	68.8 ± 0.4	24.6	84	This study
10	STKA	-31.88	141.59	43.1 ± 0.2	68.7 ± 0.6	25.6	14	This study
11	WRAB	-19.93	134.36	42.6 ± 0.3	66.0 ± 0.3	23.4	58	Chevrot et al. (1999)
12	XAN	34.03	108.92	44.4 ± 0.3	68.8 ± 0.2	24.4	54	This study

The arrival times (relative to the P -wave) of the Pds phases converted at 410 and 660 (t_{P410s} and t_{P660s}) are followed by the differential travel time $t_{diff} = t_{P660s} - t_{P410s}$, the number of stacked records, and the source of the data. Crustal corrections are applied to t_{P410s} and t_{P660s} , as in Chevrot et al. (1999); t_{diff} does not depend on the corrections.

der Hilst et al., in preparation) were constrained by means of multimode inversions of large waveform datasets (4040 and 2250 seismograms, respectively) (Fig. 6). The waveforms contained long- and intermediate-period Rayleigh waves and regional S and multiple S waves and were inverted using the partitioned waveform inversion (Nolet, 1990; Zielhuis and van der Hilst, 1996) (Australia) and the automated partitioned waveform inversion (Lebedev and

Nolet, 2000) (SE Asia). Both tomographic studies achieve dense regional-path coverage of the target regions and provide 500–600 km lateral and ~ 150 km vertical resolution in the TZ.

4.1. Resolution

The sampling with the waveform data used in the tomography is best in the upper 200 km of the mantle,

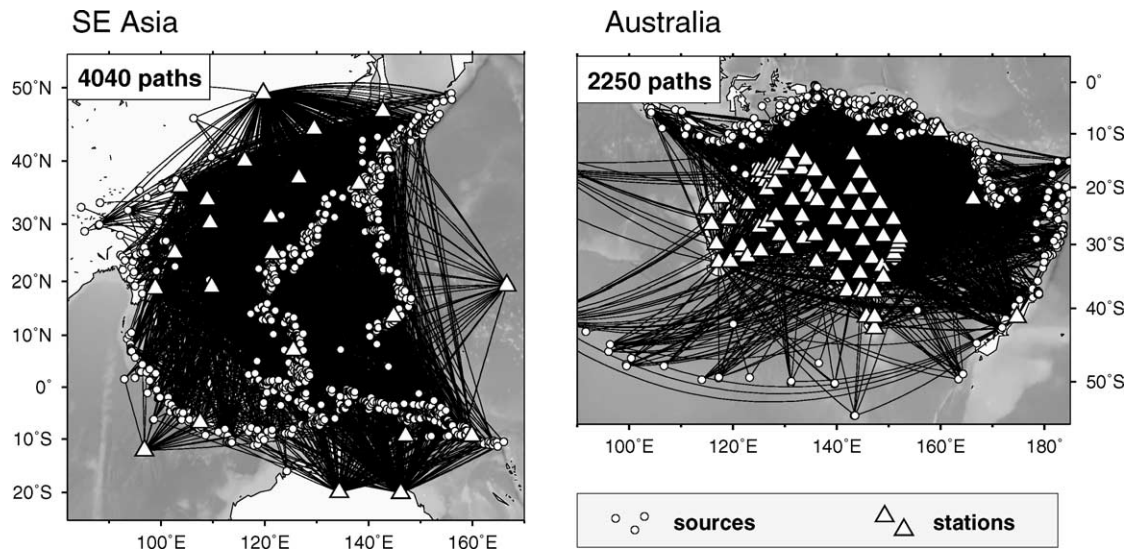


Fig. 6. Ray-path coverages used in the waveform tomography of SE Asia (Lebedev and Nolet, 2000) and Australia (Simons et al., 1999; Van der Hilst et al., in preparation).

which is also the depth range of the highest lateral heterogeneity. Here, the lateral-resolution length is 300–400 km. In a series of resolution tests, the upper 150, 200, and 300 km of the actual models were used as input patterns, with zero perturbations everywhere below. In the output of the inversions (damped and smoothed the same way as the actual data inversions) some of the more pronounced shallow anomalies were smeared down by about 100 km, but no artificial deep structure appeared, which suggests that the structure observed in the transition zone is unlikely to contain artifacts due to shallower anomalies.

The data sampling of the transition zone is weaker than that in the upper layers but still adequate for our purposes. The estimated resolution length increases to about 500 km, and anomaly magnitudes become underestimated due to damping (because the models are parameterized using regular grids and because damping parameters were chosen so that the anomalies with best data sampling were retrieved correctly, the anomalies with average sampling are overdamped). The bias, or the amount by which the magnitude is underestimated, varies spatially due to uneven data coverage and varying patterns of heterogeneity. In order to combine our converted-wave measurements with the seismic-velocity data we first attempt to correct for the magnitude bias and estimate the true S -velocity values in the upper and lower-transition-zone beneath each station of the Pds dataset.

4.2. Absolute S -velocity values

A tomographic model can be regarded as the “true” model of the subsurface passed through a “resolution filter”. The filter depends on data sampling, data quality, and the regularization of the inversion; it accounts for the differences between the tomographic model and the actual Earth structure. Ideally, we would like to find an “inverse” of the filter that would reproduce the true structure from the tomographic model.

The sensitivity volumes of long-period S waves effectively average out the perturbations at shortest wavelengths. Accounting for this, regularization of tomographic inversions included smoothness constraints on the solutions. While trying to restore the true anomaly magnitudes, we can realistically aim at obtaining a smoothed model of the true Earth structure, such that at every point in the model the

S -velocity value is an accurate average over an area with a width of a few hundred kilometers (this width is the resolution length, similar to the averaging length of Backus and Gilbert, 1968). The t_{diff} measurements average laterally over about 500 km, a width similar to the resolution length of the tomography in the transition zone. We wish to obtain robust estimates of the 500 km lateral S -velocity averages beneath the stations.

For each of the two tomographic models, we look for an “inverse filter” in the form of a set of scaling factors, one per knot of the model grid. The magnitude bias can be corrected for by multiplying the values in the tomographic model with these scaling factors. We begin the iterative search for the factors by using the actual models as input patterns for resolution tests. The models that emerge in the output of the tests are generally similar to the input, the main difference being the reduced magnitude of anomalies, especially in the transition zone. Next, we use the input/output magnitude ratios to scale up the values in the input models. Repeating the tests, we observe that the output S velocities are now closer to the ones in the actual models. This iterative procedure converges to the synthetic input models such that the output of the tests is very similar to the actual models obtained in the inversion of the data (Fig. 7).

These “best-fitting” synthetic models are our best estimate for the true upper-mantle structure beneath the regions. Further analysis, however, is needed to insure the robustness of the values beneath the stations of the Pds dataset. One major problem is the non-uniqueness of the synthetic models: there are many other models that could produce a similarly good fit. Furthermore, in poorly sampled parts, such as west-Australian TZ, the tomographic solution is constrained weakly and may depend on heterogeneity elsewhere in the model. Instead of accepting the S velocities in the “best-fitting” models as true ones, we now investigate the behavior of the scaling factors during the iterations. The general patterns of heterogeneity are similar in the input for each test, but the relative magnitude of anomalies at different locations changes from one test to another. At the stations in the western and central Australia these variations cause large fluctuations of the computed scaling factor as a function of the test input pattern. This indicates strong trade-offs between the values beneath the stations

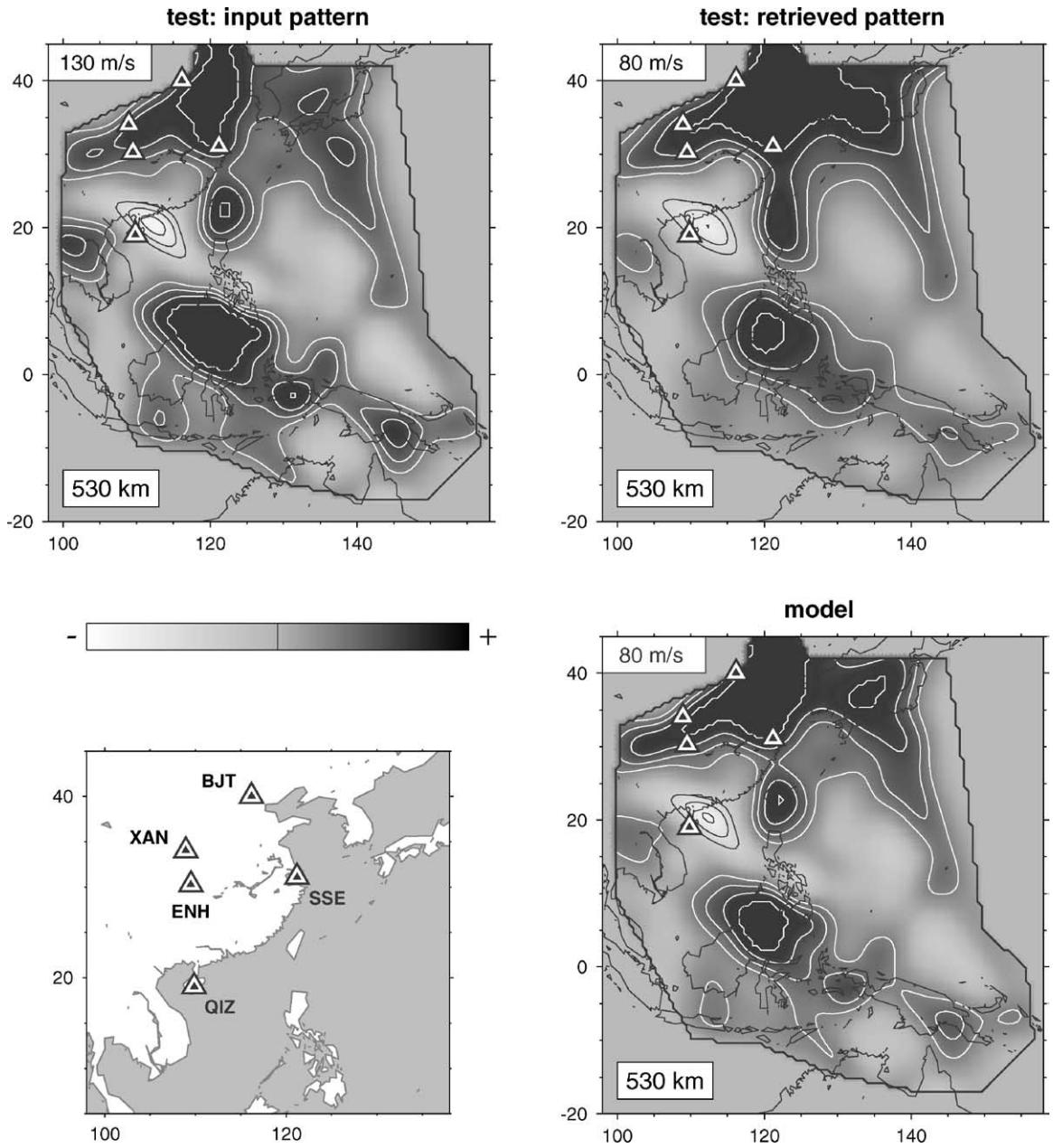


Fig. 7. An example of a resolution test for the SE Asian model. The input pattern (top left) is obtained from the actual model (bottom right) through scaling of the anomaly magnitudes, the scaling factor varying laterally. The output pattern of the test (top right) is similar to the actual model. Anomalies are plotted only in the well-sampled part of the region, bounded by the bold line. Gray-scale limits are shown in the top left corners of the frames. Stations of our data set are plotted as triangles, with the station names given on the map.

and those elsewhere in the tomographic solution and means that scaling will not produce reliable estimates. For other stations, the factors are stable, their values ranging from 1.1 ± 0.1 to 3.3 ± 0.7 .

Finally, we need to account for the fact that the a priori smoothness constraints on the Australian model were relatively weak, allowing structure with scale lengths down to 100–200 km to be present in the model. We filter out these small-scale variations using a posteriori smoothing. For each input and output model used in the iterations, a few smooth versions are computed, each with a smoothing function of a different half-width in the 300–800 km range. Small and monotonic change of the scaling factor with the smoothing width is another requirement for the Australian stations.

The requirements appeared to be severe quality criteria and were not met by all stations. Robust values for S velocities in both the upper and lower-transition-zone were obtained for eight stations (Fig. 8). The values were recomputed relative to IASP91 (Kennett and Engdahl, 1991) for a reference period of 1 s (assuming $Q = 143$ from PREM (Dziewonski and Anderson, 1981)). The upper-transition-zone anomaly ($\delta\beta_{410}$) is an average over the 410–530 km depth range; the lower-transition-zone anomaly ($\delta\beta_{660}$) is an average over the 540–660 km range. According to the standard deviations of the scaling factors, the uncertainties of $\delta\beta_{410}$ and $\delta\beta_{660}$ range from 2 to 32 m/s. We assign, however, larger, more conservative errors

of at least 30 m/s to $\delta\beta_{410}$ and 40 m/s to $\delta\beta_{660}$. The errors are assumed to be greater for the stations with greater scaling-factor variability (Fig. 8).

5. Correlation of the transition zone thickness and seismic structure

We begin the joint interpretation of our two datasets by superimposing the δt_{diff} measurements on the tomographic images of the transition zone (Fig. 9). The S -velocity anomaly plotted at each point is “scaled” as described above and averaged vertically over the TZ depth range. δt_{diff} values are plotted only for the eight stations with robust S -velocity estimates for the upper and lower TZ.

The eight points that pass all the quality tests show a good correlation between t_{diff} and seismic-velocity. If the thickness of the transition zone were constant, then the differential-time t_{diff} would be anomalously small in high-velocity regions and anomalously large in low-velocity ones. Since the observed pattern is the opposite, the thickness of the transition zone must vary and correlate positively with the seismic velocities.

We investigate the correlation quantitatively and in Fig. 10a plot the variations $\delta t_{\text{diff}} = t_{\text{diff}} - t_{\text{diff}}^{\text{iasp91}}$ (where $t_{\text{diff}}^{\text{iasp91}} = 23.9$ s) against the transition zone anomalies $\delta\beta_{\text{TZ}}$ corrected for the magnitude bias, $\delta\beta_{\text{TZ}} = (\delta\beta_{410} + \delta\beta_{660})/2$. The correlation coefficient is 0.94.

The straight line through the points was determined using a bivariate regression. Even though this was not used as a constraint for the regression, the line goes through the origin of the coordinate system within the errors (the intercept is 0.1 ± 0.4 s). This is consistent with IASP91 being an accurate average model for the transition zone beneath SE Asia and Australia.

In Fig. 10b we convert δt_{diff} into the transition zone thickness anomaly δH_{TZ} (using the reference α and β from IASP91, our $\delta\beta_{\text{TZ}}$, and $\delta \ln \beta / \delta \ln \alpha = 1.7 \pm 0.7$) and in Fig. 10c we convert $\delta\beta_{\text{TZ}}$ into temperature variations δT_{TZ} , assuming $\partial \ln \beta / \partial T = -1.35 \times 10^{-4} \text{ K}^{-1}$ from Karato (1993) and an uncertainty of the derivative of $0.4 \times 10^{-4} \text{ K}^{-1}$. The temperature δT_{TZ} and thickness δH_{TZ} of the transition zone correlate strongly, with a correlation coefficient as high as 0.98. Furthermore, the slope of the straight line through our measurement points is $-0.13 \pm 0.07 \text{ km/K}$, consistent with -0.13 km/K

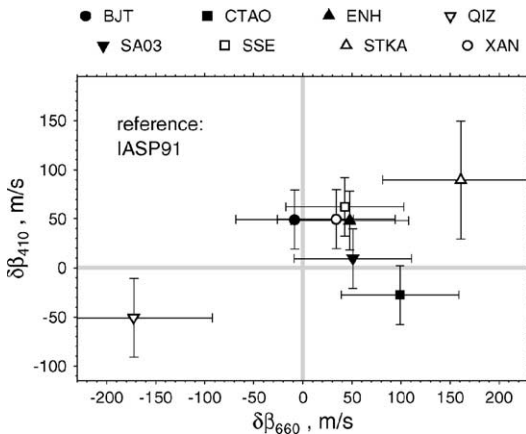


Fig. 8. The S -velocity anomaly in the upper ($\delta\beta_{410}$) and lower ($\delta\beta_{660}$) transition zone beneath the eight stations of the dataset.

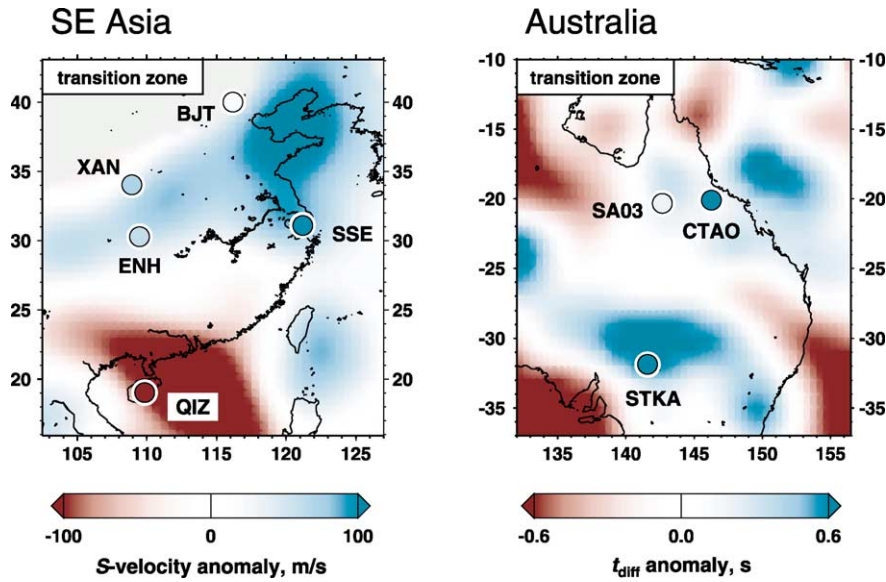


Fig. 9. Differential-time (t_{diff}) measurements compared with S -velocity anomalies estimated (scaled) from the tomographic models (see text for explanation) and averaged over the transition zone depth range. Circles denote seismic stations, with color showing measured t_{diff} anomaly. Reference S -velocity and t_{diff} values are 5335 m/s and 23.9 s, respectively, computed from IASP91 (Kennett and Engdahl, 1991).

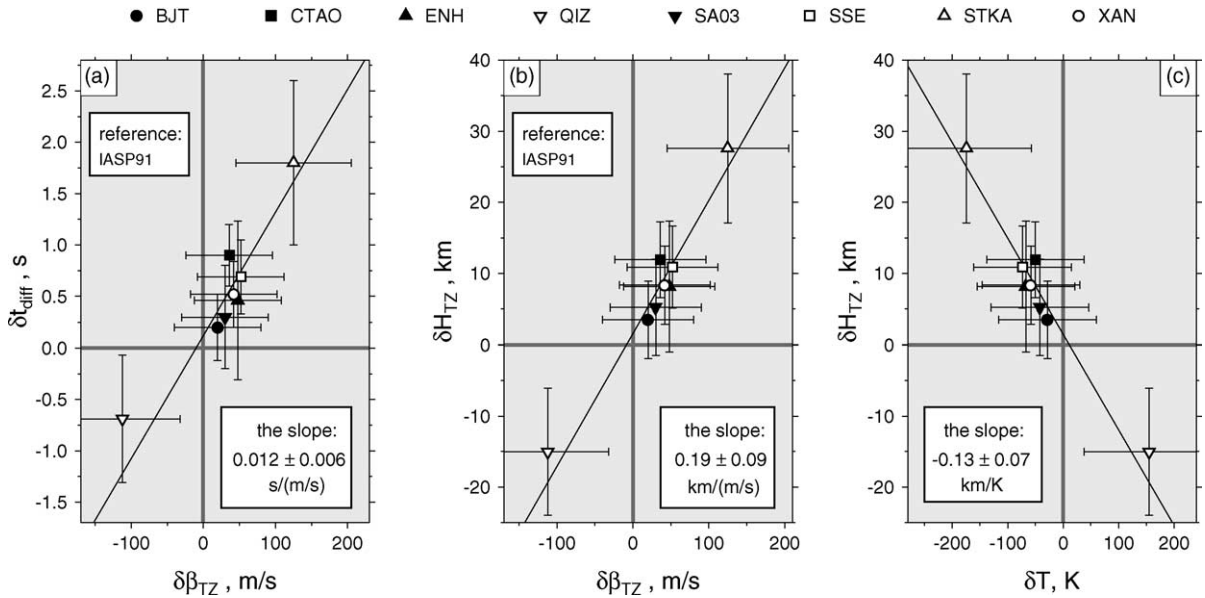


Fig. 10. Correlation between S -velocity in the transition zone ($\delta\beta_{TZ}$) and the differential-time t_{diff} (a), $\delta\beta_{TZ}$ and the computed thickness of the transition zone H_{TZ} (b), and the estimated temperature in the transition zone T_{TZ} and the thickness H_{TZ} (c). Seismic-velocity anomalies $\delta\beta_{TZ}$ are vertical averages over the transition zone depth range, and so are the estimated temperature anomalies δT_{TZ} .

computed assuming the Clapeyron slopes of the $\alpha \rightarrow \beta$ and $\text{sp} \rightarrow \text{pv} + \text{mw}$ transformations from Bina and Helffrich (1994) (2.9 and -2.0 MPa/K, respectively).

The strong correlation between t_{diff} and β_{TZ} (and thus between the TZ thickness and temperature) in SE Asia–Australia corroborates models in which phase transformations in olivine cause both 410 and 660 but appears to be at odds with the lack of correlation inferred from global models and datasets (Chevrot et al., 1999). We argue that this apparent inconsistency is due to differences in spatial resolution of t_{diff} measurements on the one hand and of α_{TZ} or β_{TZ} values from global tomography on the other. The resolution of global wavespeed heterogeneity in the TZ is most uniform at long wavelengths (Reference Earth Model Web Site: <http://mahi.ucsd.edu/Gabi/rem.html>; Becker and Boschi, 2002). However, the low (spherical harmonic) degree variations represent averages over distances (>2000 – 3000 km) that are much larger than the spatial averaging of the t_{diff} measurements (≈ 500 km). This resolution difference will obscure the actual $t_{\text{diff}} - \beta_{\text{TZ}}$ correlation if structural variations on a scale of a few hundred kilometers are present. In contrast, the t_{diff} and β_{TZ} measurements in Fig. 10a have similar lateral resolution so that the actual correlation can be measured.

We attempted to unscramble the global $t_{\text{diff}} - \beta_{\text{TZ}}$ correlation using 77 t_{diff} measurements worldwide (from the dataset of Chevrot et al. (1999), complemented by the new data reported here) and β_{TZ} values beneath corresponding stations according to the 3D mantle model S16B30 (Masters et al., 1996) (this and other global models give mutually consistent results, as detailed below). Taken at face value, the datasets correlate weakly (Fig. 11a), with a correlation coefficient $r = 0.28$. However, if we filter out short-wavelength variations of t_{diff} (by replacing the values at individual stations with a weighted average of the

values at all stations nearby) and low-pass filter the tomographic model (keeping only the largest-scale heterogeneity), the correlation increases dramatically (Fig. 11).

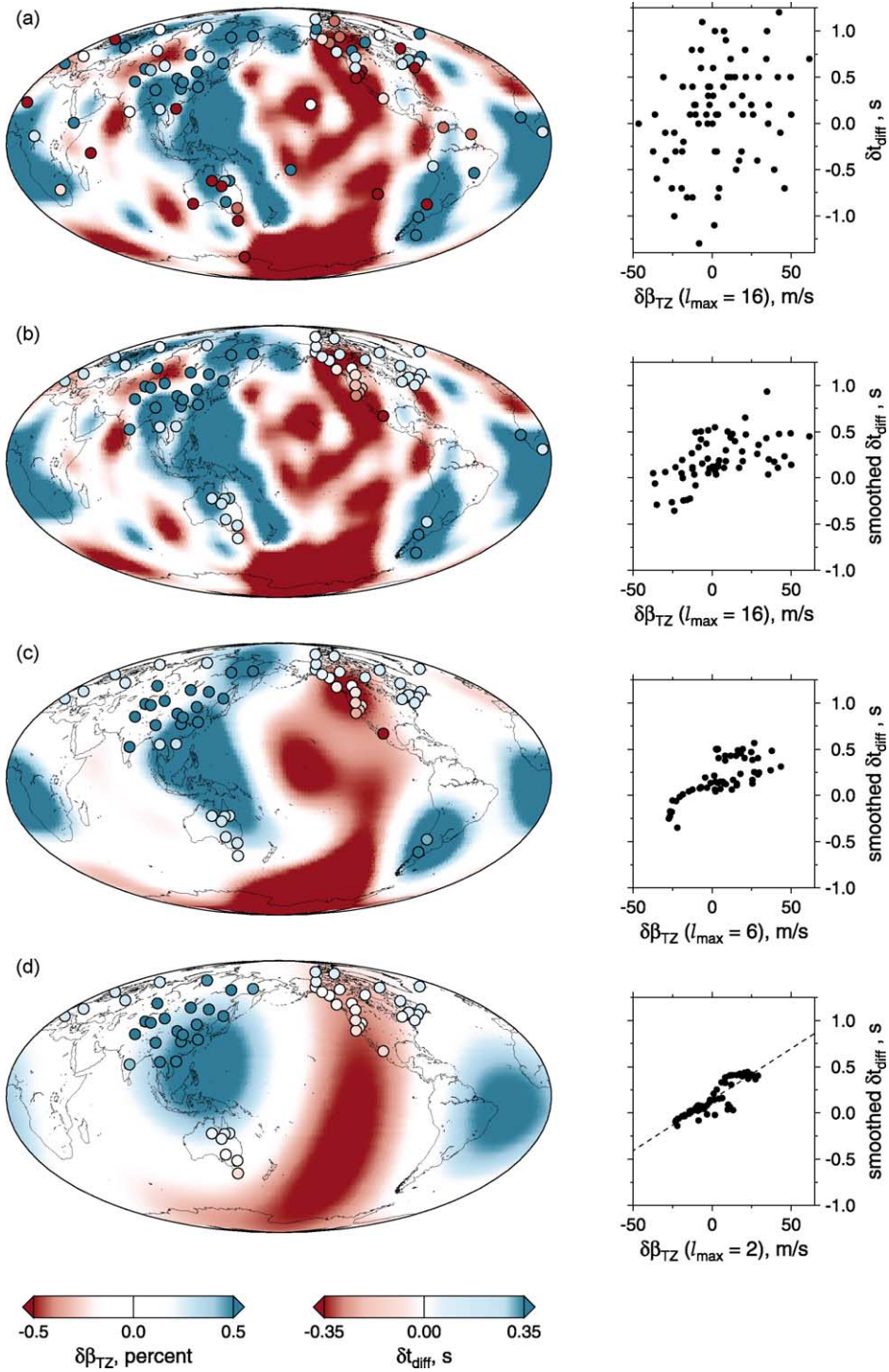
We compute the “smoothed” t_{diff} values as $\sum_i w^i t_{\text{diff}}^i / \sum_i w^i$, with the weights $w^i = \cos((\pi/2)(d^i/L_{\delta t}))$ for stations within a distance d^i smaller than the chosen averaging length $L_{\delta t}$. The accuracy of the smoothing at a station depends on the presence of nearby stations. Geographically isolated stations have to be omitted, which we implement using a threshold value w_{min} : it is required that $\sum_i w^i \geq w_{\text{min}}$.

As an alternative approach, we also expanded t_{diff} variations into spherical harmonics using the singular value decomposition. The sparseness and especially the unevenness of the geographic distribution of the measurements resulted in large uncertainties (30–100%) of the expansion coefficients, even at the lowest harmonic degrees. The spectral approach yields similar results, but because uneven data coverage is accounted for more easily in the spatial domain, we use the spatial-averaging (smoothing) scheme for the analysis.

Uneven distribution of the t_{diff} measurement points may lead to “sampling artifacts” for certain values of $L_{\delta t}$ and w_{min} . Also, our smoothing procedure introduces geographic correlation patterns into the t_{diff} dataset; low-pass filtering of tomographic models also produces a geographic correlation in β_{TZ} values. Comparing one correlation coefficient to another may thus be meaningless. However, if we vary $L_{\delta t}$ and w_{min} values in wide ranges (we use 1000–10,000 km and 2–15, respectively) and compute r for every combination of $L_{\delta t}$ and w_{min} , we can use the resulting range of r as an indicator of t_{diff} -distribution correlation with a tomographic model.

From the result of our regional studies (Fig. 10) we had expected that the global correlation would

Fig. 11. Measurements of the differential-time anomaly δt_{diff} at 77 stations around the world compared with the transition zone S -velocity anomaly $\delta\beta_{\text{TZ}}$ according to the degree-16 tomographic model S16B30 (Masters et al., 1996). Circles denote seismic stations and are filled with color showing t_{diff} anomaly. Left: δt_{diff} measurements superimposed on the 550 km cross-sections through S16B30; right: δt_{diff} measured at each station vs. $\delta\beta_{\text{TZ}}$ beneath the station. Reference t_{diff} is 23.9 s; reference β_{TZ} is the S16B30 average at 550 km. (a) Unfiltered S16B30; original δt_{diff} values. (b) S16B30 is unfiltered; δt_{diff} distribution is smoothed laterally with $L_{\delta t} = 2500$ km and $w_{\text{min}} = 1.5$; the smoothing could be done at 63 stations only (see text for explanation). (c) S16B30 is truncated at spherical-harmonic degree $l_{\text{max}} = 6$; δt_{diff} distribution is smoothed with $L_{\delta t} = 3000$ km and $w_{\text{min}} = 2.5$ (60 stations). (d) S16B30 is truncated at $l_{\text{max}} = 2$; δt_{diff} distribution is smoothed with $L_{\delta t} = 5000$ km and $w_{\text{min}} = 6$ (58 stations).



be better for the higher-degree (that is, shorter-wavelength) mantle models. Surprisingly, we observe the opposite: r generally decreases with increasing truncation degree l_{\max} of the spherical-harmonic expansion of β_{TZ} , from 0.8–1.0 with $l_{\max} = 2$ to 0.5–0.7 with $l_{\max} = 16$. Because the correlation between different global models exhibits a similar decrease with l_{\max} (Reference Earth Model Web Site: <http://mahi.ucsd.edu/Gabi/rem.html>; Becker and Boschi, 2002), we attribute this trend to larger errors in β_{TZ} at higher degrees.

The correlation of smoothed t_{diff} with other global models is similar at long wavelengths and decreases when the more uncertain shorter-wavelength β_{TZ} variations are included. With the degree-12 model S12 (Su et al., 1994) r is in the 0.5–1.0 range; with the degree-20 model S20A (Ekström and Dziewonski, 1998) $r = 0.4$ –0.6.

Comparing the “smoothed” t_{diff} heterogeneity with the best-constrained, largest-scale β_{TZ} structure ($l_{\max} = 2$), we find that t_{diff} and β_{TZ} correlate strongly (Fig. 11d). With assumed uncertainties of 0.3 s (t_{diff}) and 10 m/s (β_{TZ}), the slope of the line through the points is $0.011 \pm 0.003 \text{ s}^2/\text{m}$, consistent with the result for SE Asia–Australia in Fig. 10. Accurate uncertainty estimates for this global slope would be difficult to derive because the lateral variations of the errors in β_{TZ} are unknown and, more importantly, only a relatively small number of unevenly distributed t_{diff} data points is available. Nevertheless, Fig. 11 confirms that the thickness of and seismic velocities within the transition zone correlate not only in SE Asia and Australia but elsewhere around the world as well.

6. Discussion and conclusions

The Clapeyron slopes of the $\alpha \rightarrow \beta$ and $\text{sp} \rightarrow \text{pv} + \text{mw}$ transformations, the two reactions that apparently give rise to the 410 and 660 km discontinuities, have opposite signs and similar absolute values: 2.9 and -2.0 MPa/K , respectively, according to Bina and Helffrich (1994). This implies that variations in H_{TZ} and β_{TZ} will correlate whether or not thermal heterogeneity within the TZ is vertically coherent, that is, even if the topography on 410 does not correlate with that on 660, as proposed by Gu et al. (1998) and Flanagan and Shearer (1998).

Because

$$\delta H_{\text{TZ}} = \delta d_{660} - \delta d_{410}, \quad (1)$$

and, therefore,

$$\begin{aligned} \delta H_{\text{TZ}} = \gamma_{660} \left(\frac{\partial d}{\partial P} \right)_{660} \frac{\partial T}{\partial \ln \beta} \delta \ln \beta_{660} \\ - \gamma_{410} \left(\frac{\partial d}{\partial P} \right)_{410} \frac{\partial T}{\partial \ln \beta} \delta \ln \beta_{410}, \end{aligned} \quad (2)$$

with both the depth-pressure dependence $\partial d/\partial P$ and $\partial T/\partial \ln \beta$ similar at 410 and 660, δH_{TZ} will correlate with $(\delta \beta_{410} + \delta \beta_{660})/2$. As long as seismic velocities do not oscillate in the transition zone depth range (the condition that $\delta \beta_{\text{TZ}} \approx (\delta \beta_{410} + \delta \beta_{660})/2$), the values of δH_{TZ} and $\delta \beta_{\text{TZ}}$ should correlate and plot approximately along the straight line on Fig. 10b. Deviations from this line would be likely to signal that anomalies of non-thermal origin (in either β_{TZ} or H_{TZ}) are present in the location of the measurements and could provide insight into the mechanisms at work.

An effect of compositional transition zone heterogeneity on our observations cannot be ruled out. The values of “seismic” Clapeyron slopes may also be affected by the presence of nontransforming phases at the depth of the discontinuities (Stixrude, 1997). However, we see no evidence for this in the present datasets. Our data is consistent with compositional effects on seismic velocities and discontinuity topographies being small, or with the compositional and thermal heterogeneities having similar effects on both the shear velocity and transition zone thickness.

The maximum transition zone thickness anomaly that we observe is around 30 km, beneath the station STKA in Australia (Figs. 9 and 10). We estimate the peak-to-peak amplitude of the global δH_{TZ} variations to be ± 25 –30 km at the scale lengths of ≈ 500 km and larger. Ignoring effects of composition, this corresponds to thermal heterogeneity of around $\pm 200 \text{ K}$. A more typical range of δH_{TZ} appears to be $\pm 15 \text{ km}$ (usually, $\delta t_{\text{diff}} < 1 \text{ s}$), implying $\pm 100 \text{ K}$ variations of the transition zone temperature.

According to the smaller-scale subduction-zone studies, the huge thermal anomalies in the cold subducting lithosphere cause much larger changes in d_{410} , d_{660} , and H_{TZ} , as should be expected (e.g. Castle and Creager, 1998). In Pd_s measurements, small-scale topography on discontinuities manifests itself in

large scatter, splitting, or absence of converted-wave arrivals (Van der Lee et al., 1994). Such complexity is observed at locations both near subduction zones and away from them (Chevrot et al., 1999); the regions with strong small-scale discontinuity topography are apparently distributed among areas with smoother (≥ 500 km) variations.

The correlation of t_{diff} and β_{TZ} on both regional and global scales represents evidence in support of the view that phase transformations in olivine give rise to the 410 and 660 km discontinuities.

Acknowledgements

We thank Alet Zielhuis for running the resolution tests for the tomographic model of Australia, Oded Aharonson for carrying out the spherical-harmonic expansion of t_{diff} , the Scripps and Harvard seismology groups for making their models and software available, and Yu Gu, Hitoshi Kawakatsu, and an anonymous referee for constructive reviews. The figures were prepared with GMT (Wessel and Smith, 1995). This work was supported by the David and Lucile Packard Foundation through a Fellowship awarded to R.D. van der Hilst.

References

- Anderson, D.L., 1967. Phase changes in the upper mantle. *Science* 157, 1165–1173.
- Backus, G.E., Gilbert, F., 1968. The resolving power of gross Earth data. *Geophys. J. Roy. Astron. Soc.* 16, 169–205.
- Becker, T.W., Boschi, L., 2002. A comparison of tomographic and geodynamic mantle models. *Geochem. Geophys. Geosyst.* 3, Paper No. 2001 6C000168.
- Bernal, J.D., 1936. Geophysical discussion. *Observatory* 59, 265–269.
- Bina, C.R., Helffrich, G.R., 1994. Phase transition Clapeyron slopes and transition zone seismic discontinuity topography. *J. Geophys. Res.* 99, 15853–15860.
- Bostock, M.G., 1996. P_S conversions from the upper mantle transition zone beneath the Canadian landmass. *J. Geophys. Res.* 101, 8383–8402.
- Castle, J.C., Creager, K.C., 1998. Topography of the 660-km seismic discontinuity beneath Izu-Bonin: implications for tectonic history and slab deformation. *J. Geophys. Res.* 103, 12511–12527.
- Chaljub, E., Tarantola, A., 1997. Sensitivity of SS precursors to topography on the upper mantle 660-km discontinuity. *Geophys. Res. Lett.* 24, 2613–2616.
- Chevrot, S., Vinnik, L., Montagner, J.-P., 1999. Global scale analysis of the mantle P_d s phases. *J. Geophys. Res.* 104, 20203–20219.
- Collier, J., Helffrich, G., 1997. Topography of the “410” and “660” km seismic discontinuities in the Izu-Bonin subduction zone. *Geophys. Res. Lett.* 24, 1535–1538.
- Dueker, K.G., Sheehan, A.F., 1997. Mantle discontinuity structure from midpoint stacks of converted P to S waves across the Yellowstone hotspot track. *J. Geophys. Res.* 102, 8313–8327.
- Dziewonski, A.M., Anderson, D.L., 1981. Preliminary reference Earth model. *Phys. Earth Planet. Inter.* 25, 297–356.
- Efron, B., Tibshirani, R., 1991. Statistical data analysis in the computer age. *Science* 253, 390–395.
- Ekström, G., Dziewonski, A.M., 1998. The unique anisotropy of the Pacific upper mantle. *Nature* 394, 168–172.
- Flanagan, M.P., Shearer, P.M., 1998. Global mapping of topography on transition zone velocity discontinuities by stacking SS precursors. *J. Geophys. Res.* 103, 2673–2692.
- Goes, S., Govers, R., Vacher, P., 2000. Shallow mantle temperatures under Europe from P and S wave tomography. *J. Geophys. Res.* 105, 11153–11169.
- Gössler, J., Kind, R., 1996. Seismic evidence for very deep roots of continents. *Earth Planet. Sci. Lett.* 138, 1–13.
- Grand, S.P., van der Hilst, R.D., Widiyantoro, S., 1997. Global seismic tomography; a snapshot of convection in the Earth. *GSA Today* 7, 1–7.
- Gu, Y., Dziewonski, A.M., Agee, C.B., 1998. Global de-correlation of the topography of transition zone discontinuities. *Earth Planet. Sci. Lett.* 157, 57–67.
- Gurrola, H., Minster, J.B., 1998. Thickness estimates of the upper-mantle transition zone from bootstrapped velocity spectrum stacks of receiver functions. *Geophys. J. Int.* 133, 31–43.
- Helffrich, G., 2000. Topography of the transition zone seismic discontinuities. *Rev. Geophys.* 38, 141–158.
- Hung, S.-H., Dahlen, F.A., Nolet, G., 2000. Fréchet kernels for finite-frequency traveltimes. Part II. Examples. *Geophys. J. Int.* 141, 175–203.
- Irifune, T., Nishiyama, N., Kuroda, K., Inoue, T., Isshiki, M., Utsumi, W., Funakoshi, K., Urakawa, S., Uchida, T., Katsura, T., Ohtaka, O., 1998. The postspinel phase boundary in Mg_2SiO_4 determined by in situ X-ray diffraction. *Science* 279, 1698–1700.
- Ito, E., Takahashi, E., 1989. Postspinel transformations in the system Mg_2SiO_4 – Fe_2SiO_4 and some geophysical implications. *J. Geophys. Res.* 94, 10646–10673.
- Katsura, T., Ito, E., 1989. The system Mg_2SiO_4 – Fe_2SiO_4 at high pressures and temperatures: precise determination of stabilities of olivine, modified spinel, and spinel. *J. Geophys. Res.* 94, 15663–15670.
- Kennett, B.L.N., Engdahl, E.R., 1991. Travel times for global earthquake location and phase identification. *Geophys. J. Int.* 105, 429–465.
- Karato, S., 1993. Importance of anelasticity in the interpretation of seismic tomography. *Geophys. Res. Lett.* 20, 1623–1626.
- Lebedev, S., Nolet, G., 2000. Tomographic constraints on the structure and evolution of the SE Asian and W Pacific upper mantle. *EOS Trans. AGU* 81, S322.

- Li, X., Kind, R., Priestley, K., Sobolev, S.V., Tilmann, F., Yuan, X., Weber, M., 2000. Mapping the Hawaiian plume conduit with converted seismic waves. *Nature* 405, 938–941.
- Masters, G., Johnson, S., Laske, G., Bolton, H., 1996. A shear-velocity model of the mantle. *Phil. Trans. R. Soc. L.* 354, 1385–1410.
- Navrotsky, A., 1980. Lower mantle phase transitions may generally have negative pressure–temperature slopes. *Geophys. Res. Lett.* 7, 709–711.
- Neele, F., de Regt, H., VanDecar, J., 1997. Gross errors in upper-mantle discontinuity topography from underside reflection data. *Geophys. J. Int.* 129, 194–204.
- Nolet, G., 1990. Partitioned waveform inversion and two-dimensional structure under the Network of Autonomously Recording Seismographs. *J. Geophys. Res.* 95, 8499–8512.
- Revenaugh, J., Jordan, T.H., 1991. Mantle layering from *ScS* reverberations 2. The transition zone. *J. Geophys. Res.* 96, 19763–19780.
- Ringwood, A.E., 1969. Phase transformations in the mantle. *Earth Planet. Sci. Lett.* 5, 401–412.
- Shearer, P.M., Flanagan, M.P., Hedlin, M.A.H., 1999. Experiments in migration processing of *SS* precursor data to image upper mantle discontinuity structure. *J. Geophys. Res.* 104, 7229–7242.
- Shearer, P.M., 2000. Upper mantle seismic discontinuities. In: Karato, S., Forte, A.M., Liebermann, R.C., Masters, G., Stixrude, L. (Eds.), *Earth's Deep Interior: Mineral Physics and Tomography From the Atomic to the Global Scale*. AGU, Geophys. Monograph, 117, 115–131.
- Shim, S.-H., Duffy, T.S., Shen, G., 2001. The post-spinel transformation in Mg_2SiO_4 and its relation to the 660-km seismic discontinuity. *Nature* 411, 571–574.
- Simons, F.J., Zielhuis, A., van der Hilst, R.D., 1999. The deep structure of the Australian continent from surface-wave tomography. *Lithosphere* 48, 17–43.
- Stixrude, L., 1997. Structure and sharpness of phase transitions and mantle discontinuities. *J. Geophys. Res.* 102, 14835–14852.
- Su, W.-J., Woodward, R.L., Dziewonski, A.M., 1994. Degree 12 model of shear velocity heterogeneity in the mantle. *J. Geophys. Res.* 99, 6945–6980.
- Suito, K., 1977. Phase relations of pure Mg_2SiO_4 up to 200 kilobars. In: Manghnani, M., Akimoto, S. (Eds.), *High-Pressure Research: Applications in Geophysics*. Academic Press, San Diego, CA, 255–266.
- Van der Hilst, R.D., Kennett, B., Christie, D., Grant, J., 1994. Project SKIPPY explores the lithosphere and mantle beneath Australia. *EOS Trans. AGU* 75, 177, 180–181.
- Van der Hilst, R.D., Widiyantoro, S., Engdahl, R.E., 1997. Evidence for deep mantle circulation from global tomography. *Nature* 386, 578–584.
- Van der Lee, S., Paulssen, H., Nolet, G., 1994. Variability of *P*660s phases as a consequence of topography of the 660-km discontinuity. *Phys. Earth Planet. Inter.* 86, 147–164.
- Vidale, J.E., Benz, H.M., 1992. Upper-mantle seismic discontinuities and the thermal structure of subduction zones. *Nature* 356, 678–683.
- Vinnik, L.P., 1977. Detection of waves converted from *P* to *SV* in the mantle. *Phys. Earth Planet. Inter.* 15, 39–45.
- Weidner, D.J., Wang, Y., 2000. Phase transformations: implications for mantle structure. In: Karato, S., Forte, A.M., Liebermann, R.C., Masters, G., Stixrude, L. (Eds.), *Earth's Deep Interior: Mineral Physics and Tomography From the Atomic to the Global Scale*. AGU, Geophys. Monograph, 117, 215–235.
- Wessel, P., Smith, W.H.F., 1995. New version of the generic mapping tools released. *EOS Trans. AGU* 76, 329.
- Wicks, C.W., Richards, M.A., 1993. A detailed map of the 660-kilometer discontinuity beneath the Izu-Bonin subduction zone. *Science* 261, 1424–1427.
- Zhao, L., Jordan, T.H., Chapman, C.H., 2000. Three-dimensional Fréchet differential kernels for seismic delay times. *Geophys. J. Int.* 141, 558–576.
- Zielhuis, A., van der Hilst, R.D., 1996. Upper-mantle shear velocity beneath eastern Australia from inversion of waveforms from SKIPPY portable arrays. *Geophys. J. Int.* 127, 1–16.